Project Report
LSP-245

Selective Laser Melting of Metal Matrix Composites: FY18 Advanced Materials & Processes Line-Supported Program

E.M. Parsons
T.M. Mower

8 February 2019

Lincoln Laboratory
MASSACHUSETTS INSTITUTE OF TECHNOLOGY
LEXINGTON, MASSACHUSETTS

This material is based upon work supported by the Assistant Secretary of Defense for Research and Engineering under Air Force Contract No. FA8702-15-D-0001.

This report is the result of studies performed at Lincoln Laboratory, a federally funded research and development center operated by Massachusetts Institute of Technology. This material is based upon work supported by the Assistant Secretary of Defense for Research and Engineering under Air Force Contract No. FA8702-15-D-0001. Any opinions, findings, conclusions or recommendations expressed in this material are those of the author(s) and do not necessarily reflect the views of the Assistant Secretary of Defense for Research and Engineering.

Massachusetts Institute of Technology
Lincoln Laboratory

Selective Laser Melting of Metal Matrix Composites: FY18 Advanced Materials & Processes Line-Supported Program

E.M. Parsons
T.M. Mower

Group 74

Project Report LSP-245

8 February 2019

Lexington Massachusetts

This page intentionally left blank.

ABSTRACT

The capabilities of prototypes can be substantially enhanced by increasing the performance of the structural components that protect and support the payload. At MIT LL, the engineering of these components is particularly challenging because lead times are short, deformations in precision systems must be minimal, and prototypes face a range of environments, ranging from high shock and vibration loads during deployment to extreme and variable temperatures during operation. Structural performance can be improved, while simultaneously decreasing system cost and complexity, by using lightweight structural materials with a high ratio of elastic modulus to mass density, or specific stiffness. However, materials presently suitable for fabrication of prototypes all exhibit unremarkable specific stiffness. Reinforcing a ductile metal with ceramic particles results in a composite material, commonly called a metal matrix composite (MMC), that superimposes the toughness of the metal with the stiffness and thermal stability of the ceramic. Although improvements in specific stiffness of over 100% are possible, MMCs are almost never used in prototypes because they require long lead times and cannot be shaped into complex geometries with existing methods. This document describes progress toward developing aluminum matrix composites that can be processed with selective laser melting (SLM), a 3D printing method that uses a high intensity laser to consolidate thin layers of metal powder. Feedstock powders are being developed specifically for the SLM process, and laser consolidation is being conducted with a custom built SLM testbed that allows process parameters to be broadly tuned to prevent defects and produce optimal microstructures. The goal of the program is to transfer the materials and methods to commercial SLM machines at MIT LL and other organizations, enabling materials with high specific stiffness to be used for the first time in components requiring short lead times and complex shapes.

This page intentionally left blank.

TABLE OF CONTENTS

This page intentionally left blank.

LIST OF FIGURES

LIST OF FIGURES
(Continued)

LIST OF FIGURES

(Continued)

This page intentionally left blank.

1. SELECTIVE LASER MELTING OF METAL MATRIX COMPOSITES: INTRODUCTION

Additive manufacturing (AM) or "3D printing" has had big impact on numerous sectors at scales ranging from microfabrication to big area manufacturing (size of meters). Many predict that it will soon be recognized as the technology behind the third industrial revolution. It is defined by the ISO/ASTM as "the process of joining materials to make parts from 3D model data, usually layer upon layer, as opposed to subtractive and formative manufacturing methodologies." With additive manufacturing, parts of complex geometry can be built with a single machine operation and without any special masks, tooling, dies, or fixtures. Originally used primarily for fabrication of prototypes and models of design concepts, various additive manufacturing methods are presently capable of producing functional devices, components, and structures constructed from a range of material types. In fact, data published in the 2017 Wohlers Report show that the most common use of additive manufacturing is the fabrication of functional parts (33.8% of applications, and 60.6% of the market for an estimated $3.6 billion).

The first and most advanced application of 3D printing technology is the production of polymer parts. Via extrusion, photopolymerization, or fusion, parts can be fabricated from a variety of different polymers, including thermoplastics, thermosets, and polymer matrix composites. With vat polymerization, build resolution can be as good or better than it is with conventional fabrication methods ($< 1-2\,\mu$m with microstereolithography and about 50 nm with two-photon polymerization).

3D printing of metals has been much slower to develop than printing of polymers has been, but production of final parts by printing of metals is now increasing rapidly. The most common and highest resolution form of metal printing is selective laser melting (SLM), a powder bed fusion process in which selective areas of a powder bed are melted and fused with a high energy laser (Figure 1). Once fusion of a given layer is complete, the build platform is lowered, and another layer is spread or "recoated" over the platform. A similar process, selective laser sintering (SLS), can be used to fuse ceramics by sintering—not full melting. SLM has recently been adopted by MIT LL and is ideal for the production of low volumes of high value parts, typical of the defense and aerospace sectors. Heavily light-weighted parts and parts with internal channels or cavities can be manufactured, sometimes reducing to a single piece an assembly that would otherwise consist of dozens of separate components joined together. In many cases, SLM enables fabrication of parts with complex features that could not be produced at all with conventional methods.

Despite the explosive growth and many recent success stories in the additive manufacturing sector, use of AM for fabrication of critical structural components has been limited because the material properties of existing AM materials are insufficient. At MIT LL, we increasingly need high performance metals to meet the demands of prototypes that are subject to a range of thermal and mechanical loads during deployment and operation. In particular, many prototypes include components that require complex 3D shapes, high stiffness, high thermal stability, and low mass.

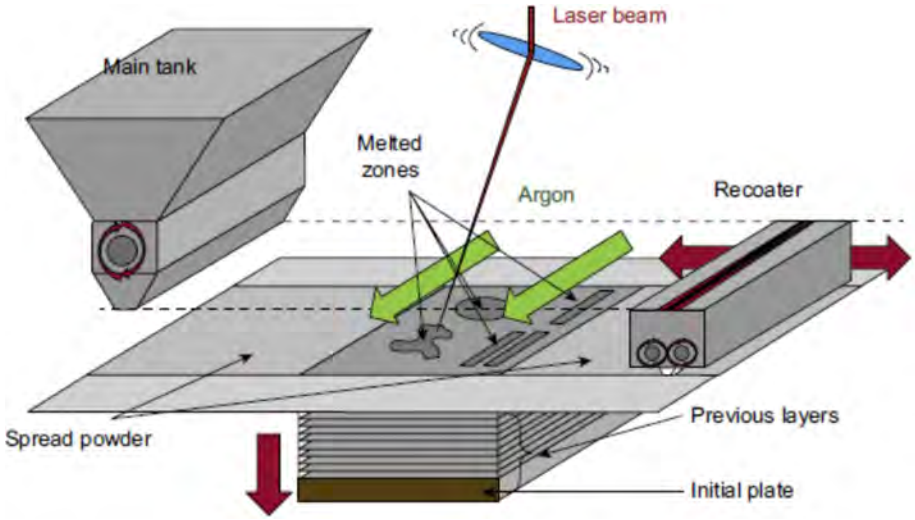

Figure 1. Schematic of the build chamber of a selective laser melting machine, showing the laser beam, build plate, powder recoater, and flow of inert gas. This example uses a hopper to deposit powder (top left), similar to the design of the micro-SLM.

Although selective laser melting can produce parts with unmatched geometric complexity, fabrication with SLM is presently limited to just a few alloys that exhibit unremarkable mechanical properties. For example, the only aluminum alloys widely used with SLM are Al-Si10-Mg and Al-12Si. These alloys are designed for casting and exhibit yield strength, ductility, and fatigue strength substantially inferior to the properties of commonly used wrought alloys such as aluminum 2024, 6061, and 7075. In other cases, for a particular alloy composition, processing with SLM results in a fused material with mechanical properties that fall short of the properties of the wrought material.

In this program, we therefore seek to develop metals for SLM that exhibit properties superior to the properties of the materials that are currently available for use in prototypes. It is well known that the properties of plain metals fabricated by traditional methods can be improved dramatically by the introduction of well-dispersed ceramic particles, forming a metal matrix composite (MMC). MMCs can exhibit specific stiffness and strength nearly double those of the unreinforced metal, and the presence of the ceramic phase also improves dimensional stability and fatigue strength. However, existing MMCs are rarely used in prototypes because they require long lead times and are nearly impossible to shape into complex geometries with existing methods. The hard ceramic phase causes machining of MMCs to be slow and difficult, limiting the use of MMCs to structures that can be cast, extruded, or forged to near net shape. Fabricating MMC components with additive manufacturing would be an ideal solution, but research toward this goal has only recently begun, with few results published, and no suitable MMCs are commercially available for additive manufacturing. Here, we describe progress toward developing MMCs specifically for SLM, using

a bottom-up approach that starts by considering the elemental composition and properties of the feedstock powder.

This page intentionally left blank.

2. DEVELOPMENT OF FEEDSTOCK POWDERS

For feedstock powder, SLM requires thin, homogeneous layers of fine metal particles that are tightly packed. Not only do thin layers and small particles improve print resolution, but they are necessary to ensure adequate fusion between layers. The laser must be able both to melt fully the current layer and to penetrate into previously fused layers. Because the depth of laser penetration and the depth of the melt pool are proportional to the spot size of the laser beam, the layer thickness must scale with the diameter of the beam ($\sim 100\,\mu$m).

Unlike the few prior efforts to develop MMCs for SLM, we are designing constitutive materials and processing methods specifically for both SLM conditions and for the critical LL material requirements of stiffness and ductility. (Most prior work has focused on abrasive wear, strength, and low ceramic content, using existing MMC compositions.) For the matrix metal, we focus on aluminum alloys because they meet the common MIT LL requirements of low density, high thermal diffusivity, and good corrosion resistance. Specifically, we start with an aluminum alloy powder designed for SLM processing, Al-Si10-Mg. For the ceramic reinforcement, we begin with the recognition that, to form a stiff, strong, and ductile composite, particles must be evenly distributed, strongly bonded to the matrix, and small (defect-free, $\sim 1\,\mu$m). Alumina (Al_2O_3) or silicon carbide (SiC) are most often used in MMCs because they are readily available at low cost, but we determined that titanium diboride (TiB_2) is much more appropriate for SLM processing because of the nature of its chemical and physical interactions with molten aluminum.

The properties of the fused material depend, not only on the composition of the powders, but also on the properties of the powder bed. In order to minimize the porosity and surface roughness of the fused material, the uniformity and packing density of the powder bed should be maximized. Variations in layer thickness, packing density, and distributions of particle size or shape can destabilize the melt pool. These instabilities frequently lead to discontinuous or rough melt tracks that cause porosity, weak interlayer bonding, and poor surface finish. Increasing the packing density improves the thermal conductivity of the powder bed, promoting uniform heating and reducing vaporization that can cause loss of alloying elements and the formation of large pores (keyhole pores). Furthermore, with increases in packing density come also decreases in the consolidation strains that accompany melting and increases in the load bearing capacity of the unfused powder, thereby reducing residual stresses and part distortions.

2.1 PHYSICAL CHARACTERISTICS OF RAW POWDERS

Al-Si10-Mg is by far the most common aluminum alloy used with SLM. In unreinforced form, the consolidated alloy exhibits good, but not exceptional, stiffness ($E \approx 69\,$GPa), strength ($\sigma_y \approx 250\,$MPa), and toughness ($e_f \approx 10\%$). The processing of Al-Si10-Mg by SLM is reasonably well understood: The elevated silicon content causes the melt to have high fluidity and minimizes the shrinkage that can lead to hot tearing during solidification. Furthermore, the magnesium breaks

up the surface aluminum oxide layers and lowers the surface tension of the melt and also enables precipitation hardening by natural or artificial aging.

Gas atomized Al-Si10-Mg powders of different sizes from several different powder manufacturers were considered (Table 1). Gas atomization is commonly used to manufacture powders for powder bed fusion because it produces reasonably spherical particles at an affordable cost. The elemental compositions of the powders were nearly identical, but the morphology of the powders differed substantially. Of the standard SLM powders with $d_{50} \sim 35\,\mu$m, the powder from Valimet was the most spherical and smallest in diameter, while the powder from LPW was the least spherical and largest in diameter (Table 1 and Figure 2). The plain powders all exhibit apparent densities in the range of 1.3–1.4 g/cm^3, with apparent density increasing with increasing particle size and sphericity. Small and angular particles pack poorly compared to large, spherical particles because of the effects of interparticle interference, friction, and cohesive forces.

TABLE 1

Summary of Al-10Si-Mg SLM Powder Elemental Composition and Particle Size Distribution ($\rho_{\text{solid}} = 2.68\,\text{g/cm}^3$)

	Composition (wt%)				Particle size (μm)			Apparent
Powders	**Al**	**Si**	**Mg**	**Fe**	**d10**	**d50**	**d90**	**ρ (g/cm^3)**
ECKA Standard	n/a	n/a	n/a	n/a	26 nom.	n/a	63 nom.	1.363
Valimet Standard	Bal	10.45	0.30	0.17	15.74	28.91	50.58	1.335
Valimet Coarse	Bal	10.23	0.35	0.18	23.24	41.70	66.48	1.383
LPW Standard	Bal	9.90	0.38	0.09	> 20	40.28	< 63	1.300
LPW Coarse	Bal	9.50	0.32	0.21	70.34	85.02	103.7	1.341

Titanium diboride was chosen as the ceramic reinforcement because of its excellent physical properties and inertness when in contact with molten aluminum at high temperatures. TiB_2 is nearly eight times stiffer than aluminum ($E = 530{-}565\,\text{GPa}$) and over ten times as hard (25–35 GPa Vickers). It has a high melting point ($T_\text{m} = 2790{-}3225\,^\circ\text{C}$), low solubility in liquid aluminum at high temperature (1.21×10^{-8} at 960 °C), and very low reactivity with aluminum, minimizing the risk of forming brittle intermetallic phases. Furthermore TiB_2 and aluminum have physical properties that favor particle engulfment, epitaxial growth, wetting, and strong interfacial bonding. (The Hamaker constant of TiB_2 characterizing the nature of the repulsive van der Waals

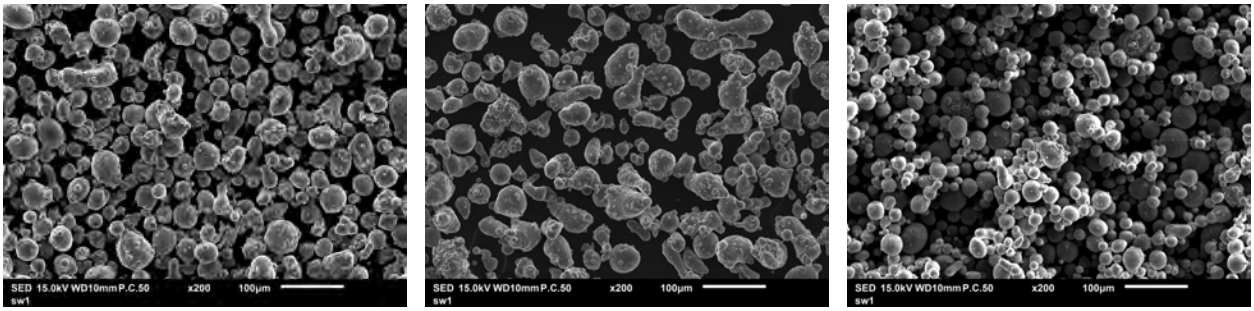

(a) (b) (c)

Figure 2. SEM images of gas atomized Al-Si10-Mg SLM powders from various manufacturers: (a) ECKA Granules; (b) LPW standard; (c) Valimet standard. The powders show occasional rod-shaped particles. The Valimet powder (c) has the smallest and most spherical particles, and the LPW powder has the largest and least spherical particles (b).

forces is close to that of molten aluminum, and the two materials have crystallographic orientation relationships that minimize the solid-particle interfacial energy.) We purchased several different powders from U.S. Research Nanomaterials and H.C. Starck (Table 2) with particle sizes in the range of 1–10 μm—about an order of magnitude smaller than the size of the Al-Si10-Mg particles. The various powders were chosen so that we could investigate the effect of particle size distribution (PSD), shape, and elemental composition (namely, carbon and oxygen content). Manufactured by crushing or grinding, the TiB_2 particles are angular and faceted but approximately equiaxed in shape (Figure 3). The 0.2−5.0 μm particles from H.C. Starck, in particular, exhibit a strong tendency to agglomerate because cohesive forces exceed gravitational forces at this particle size.

2.2 PRODUCTION OF COMPOSITE POWDERS

In this section, we describe the development of powders that are a composite of Al-Si10-Mg and TiB_2. The first goal was to produce powders that are a homogeneous mixture of the two materials in order to maximize the likelihood that the ceramic will be evenly distributed in the consolidated composite. Agglomeration of the TiB_2 particles must be avoided because brittle fracture of MMCs often initiates within clusters of reinforcements, where high levels of hydrostatic stress cause voids to form in the metal. The second goal was to produce composite powders with good flow characteristics so that thin, uniform layers of the powder can be spread over the build plate of the SLM machine. Composite powders were produced by two methods: pure blending and mechanical alloying.

TABLE 2

Summary of Titanium Diboride Physical Characteristics

	Composition (wt.%)					Particle size (μm)		
Powders	**Ti**	**B**	**C**	**O**	**Fe**	**d10**	**d50**	**d90**
U.S. Nano	> 67.5	> 30.50	< 1.5	< 1	< 0.2	2 nom.	n/a	12 nom.
H.C. Starck D	Bal	30.6	0.2	0.8	0.03	1.3	5.1	8.9
H.C. Starck F	Bal	31.1	0.1	0.9	0.0	0.7	2.9	5.0
H.C. Starck SE	Bal	30.7	0.3	0.9	0.0	1.0	4.6	8.5

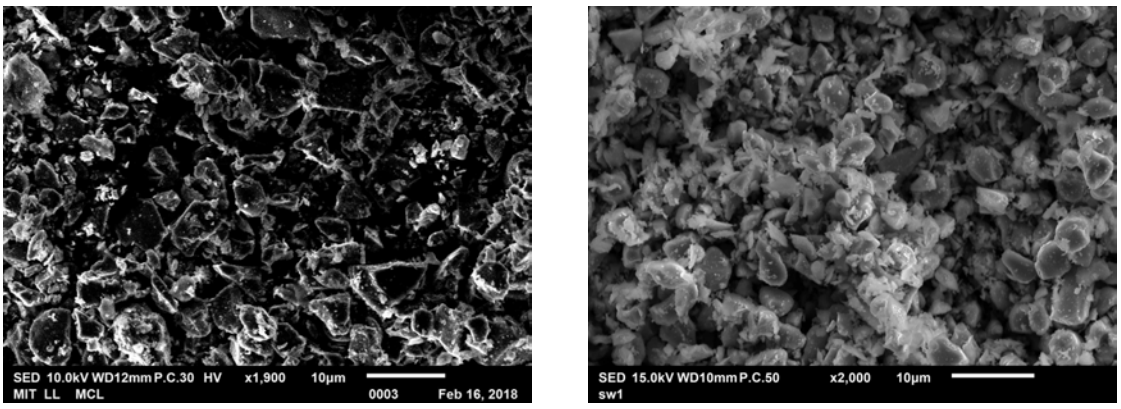

(a) (b)

Figure 3. SEM images of titanium diboride microparticles: (a) U.S. Research Nanomaterials; (b) H.C. Starck, Grade F. The particles exhibit angular shapes, with sizes in the range of 1–10 μm.

2.2.1 Blended Composite Powders

Aluminum and ceramic powders were gently dry blended in a shaker mixer (Glen Mills Turbula T2F). The powders were first dried for 16 h at 80 °C. Then, the mixer's stainless steel vial was filled under argon with 1080 g of Al-Si10-Mg and 120 g of TiB_2, and the powders were mixed for 16 h at 60 rpm. We handled, mixed, and stored the powders under argon in order to prevent the formation of oxides that are well known to cause defects in laser consolidated materials. Blends of various Al-Si10-Mg and TiB_2 powders were produced, and all blends exhibited even distribution

of the two phases. Furthermore, there was no evidence that the aluminum particles were deformed by the mixing process. (Figure 4 shows a typical blended powder.)

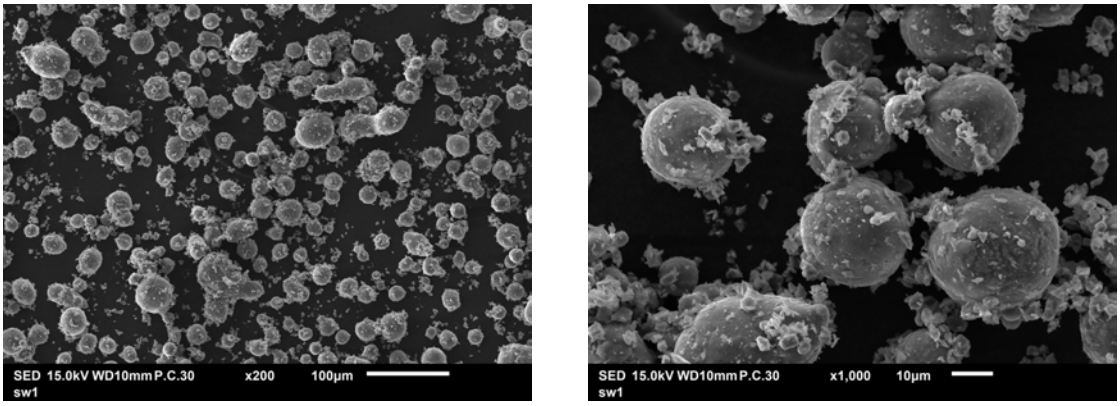

(a) (b)

Figure 4. Composite powders fabricated by mechanical blending: Valimet Al-Si10-Mg standard powder mixed with H.C. Starck Grade F powder at 10 wt% ceramic: (a) 200× magnification; (b) 1000× magnification.

2.2.2 Mechanically Alloyed Composite Powders

Composite powders were also manufactured by mechanically alloying in a planetary ball mill (Fritsch PULVERISETTE 6 Premium). Mechanical alloying is a high energy, solid state process that can produce homogeneous mixtures of multiple materials at or below the microscale. In a planetary mill, two steel or ceramic vials are loaded with the powders to be alloyed and balls made from a material identical to that of the vials. The vials are then secured to a disc that rotates at high speed during milling, while the vials spin in the opposite direction about their own axes at an angular speed of about twice the rate of disc rotation (Figure 5a). The impacts between the balls and the inner walls of the vials cold weld and fracture intervening particles such that the final milled powder is composed of particles that are each a composite or alloy of the starting powders. Here, as illustrated in Figure 5b, the goals were to create ceramic-reinforced aluminum particles that are equiaxed and similar in size to the starting aluminum powder. We hypothesize that the uniform mixture of aluminum and ceramic, with intimate contact even in the solid state, will ensure distribution and wetting of the ceramic particles during laser consolidation. Furthermore, the monodisperse particle size distribution that is typical of mechanically alloyed powders should optimize the flow characteristics of the composite powder.

Mechanical alloying is characterized by numerous process variables that control the properties of the alloyed powder. For given disk and vial diameters, the mass of each ball and the speed of

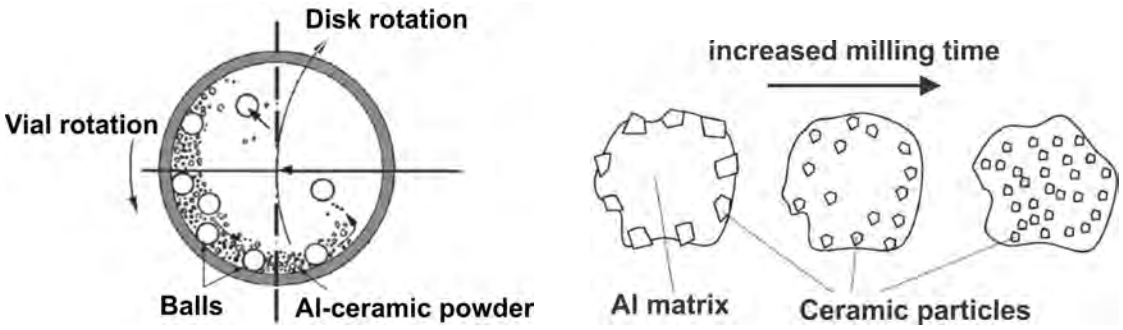

Figure 5. Schematic of process to form composite particles by mechanical alloying (ball milling): (a) Impacts between the balls and between balls and the vial cause plastic deformation, cold welding, and fracture of the aluminum particles; (b) As the milling time increases, the ceramic particles decrease in size and become evenly distributed within the aluminum particles.

the mill determine the energy per impact, E_b, while the size of each ball and the fill ratio of the vial primarily affect the efficiency of the process. A combination of these parameters determines the milling time required. The process variables held constant are summarized in Table 3.

Additional critical alloying parameters are the selection of process control agent (PCA), if any, and its mass fraction. Nearly always used in the mechanical alloying of aluminum, PCAs are organic compounds that adsorb on the surface of the particles, reducing their surface energy and therefore decreasing the driving force for cold welding. Because initial experiments without PCA showed excessive cold welding and no evidence of fracture, we chose to use a PCA for this process.

While experimenting with many different process parameters, we determined a range of parameters that produce composite particles with the desired properties. These parameters are mill speeds of 320–450 rpm, ratio of ball mass to powder mass (BPR) of 10, vial fill ratio of about 0.55, ball diameter of 10.3 mm or 20 mm, and a PCA mass fraction of 2 wt%. In the alloying trials described here, 110 g of blended Al-Si10-Mg + 10 wt% TiB_2 powder was added to each vial, together with 2 wt% PCA. Depending on the mill speed, the mill was run for periods of 2–4 min, followed by rest periods of 10 min. The rest periods were designed to prevent excessive increases in temperature that would suppress the yield strength of the aluminum below the stress required to cause fracture. During rest periods, we sampled the powder at regular intervals for examination by optical microscopy, SEM, and statistical analysis.

The successful alloying trials exhibited trends that are characteristic of the mechanical alloying of most ductile metals. Figure 6 shows a typical result with 10 mm balls, starting with a blend of LPW Standard aluminum powder and U.S. Nano TiB_2 powder. Initially, the ductile aluminum

TABLE 3

Fixed Mechanical Alloying Parameters

Parameter	**Property**	**Value**
Disc wheel	Effective radius, r_d	90 mm
Vial:disc velocity, $\omega_\mathrm{v} : \omega_\mathrm{d}$		-2:1
Milling vials	Volume	500 mL
	Material	440C stainless steel
	Radius, r_v	45 mm
	Height, h_v	84.6 mm
Balls (here)	Material	440C stainless steel
	Total mass	1100 g
Powder (here)	Total mass, m_p	110 g
	wt% TiB_2	10%

particles plastically deform and weld to each other, forming large plate-like particles (Figure 6 b,c). Then, between 120 min and 180 min of milling, the aluminum strain hardens to an extent that brittle fracture can occur, and the particles begin to decrease in size and become more spherical (Figure 6 d,e). After 240 min of milling, the alloyed particles are similar in size to the starting aluminum powder and approximately equiaxed. At this time, welding and fracture may have reached a state of equilibrium.

Decreasing the mill speed to 320 rpm decreases both the energy per impact and the frequency of impacts. As a result, after 240 min of milling, the particles are still large and flat (Figure 7). At this speed, additional milling time is required for fracture to occur, assuming that the impact energy is adequate to cause fracture eventually. The advantage to milling at low speed is that the temperature rise of the material will be lower than it is at high speed, potentially causing welding and fracture to equilibrate at a smaller particle size.

Quantitative particle analyses conducted with a Malvern Morphologi G3 confirm the SEM observations and characterize the effects of ball size and type of PCA (Figure 8). At short milling times, when plastic deformation and cold welding are dominant, the average particle diameter by volume, d_{50}, increases. After longer periods of milling, fracture becomes prevalent and the particle size decreases. The trend in number of particles per sample is less clear, but generally the number of particles decreases with increasing milling time, as fracture competes with both cold welding of the

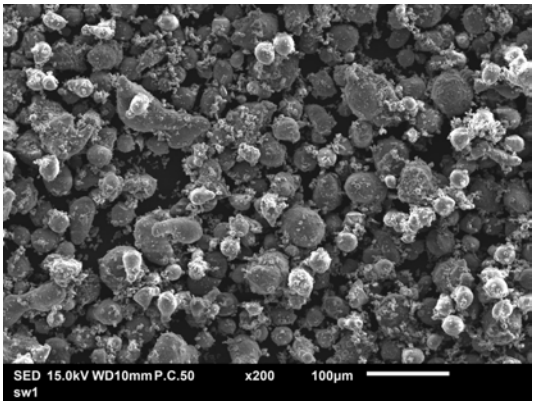

(a)

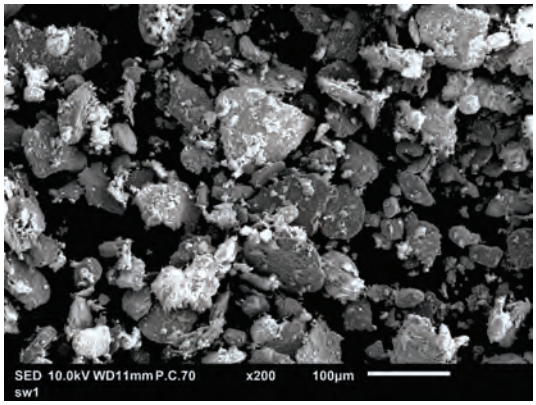

(b)

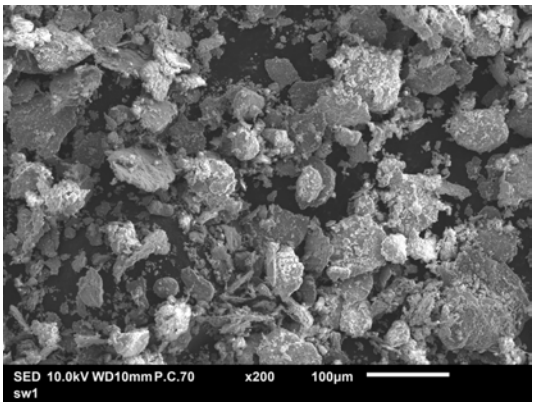

(c)

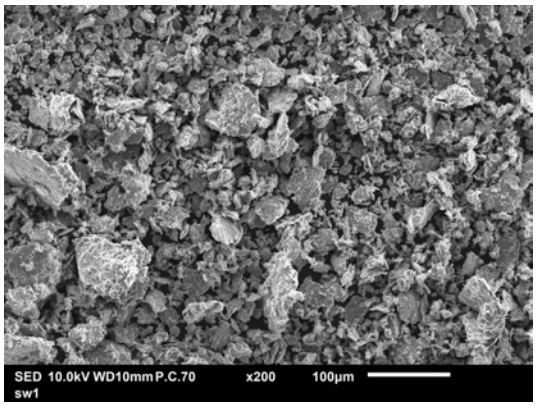

(d)

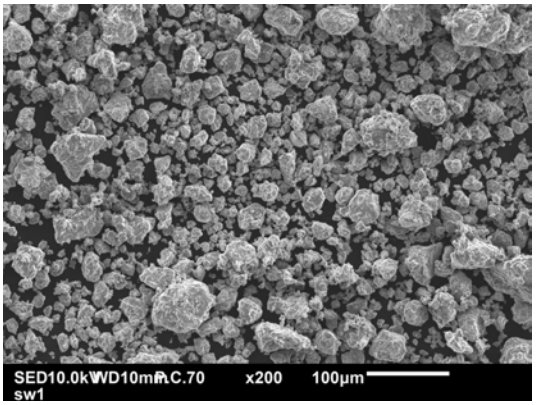

(e)

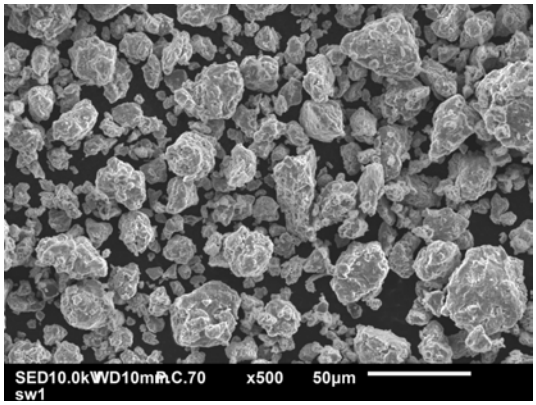

(f)

Figure 6. High speed ball milling of LPW Al-Si10-Mg standard powder with U.S. Nano TiB_2 powder at 10 wt% ceramic: (a) Starting blend; (b) t=60 min; (c) t=120 min; (d) t=180 min; (e) t=240 min; (f) t=240 min at high magnification. (Mill speed=450 rpm, d_b = 10.3 mm, BPR=10, PCA: stearic acid at 2 wt%.)

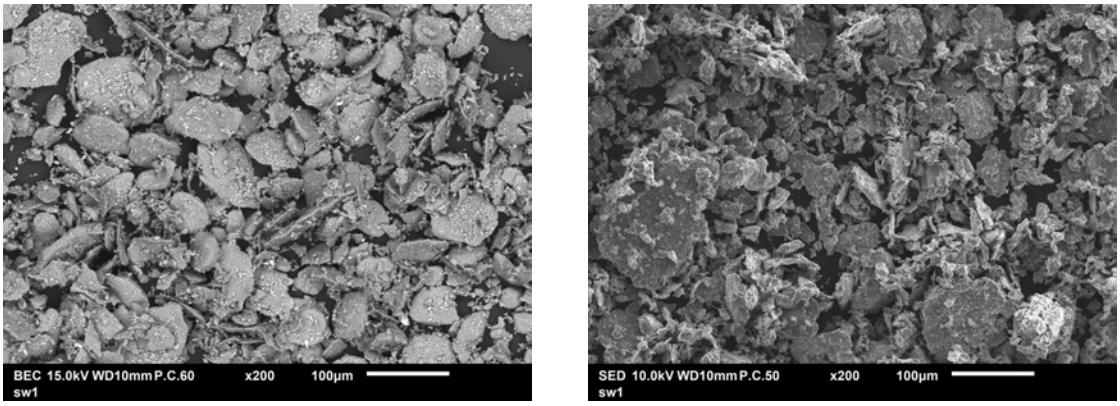

(a) (b)

Figure 7. Moderate speed ball milling of LPW Al-Si10-Mg standard powder with U.S. Nano TiB_2 powder at 10 wt% ceramic: (a) t=240 min with ball diameter d_b=10.3 mm; (b) t=240 min with ball diameter d_b=20 mm. (Mill speed=320 rpm, BPR=10, PCA: stearic acid at 2 wt%.)

aluminum and alloying of the two phases (i.e., the ceramic particles are consumed by the aluminum). At a fixed mill speed of 450 rpm, increasing the diameter of the balls from 10.3 mm to 20 mm does not significantly affect the results at $t = 120$ min. However, the particles temporarily grow larger than they do with 10.3 mm balls due presumably to the increase in temperature that accompanies the large increase in energy per impact ($E_b \propto d^3$). The type of PCA did not significantly affect the results. In future production, only stearic acid will be used because it can be conveniently handled inside a glovebox with inert atmosphere.

Finally, sectioning of the ball milled powders confirmed that alloying of the Al-Si10-Mg and TiB_2 was successful. The SEM images in Figure 9 demonstrate that each alloyed particle consists of an aluminum matrix uniformly modified with $\sim$1 μm TiB_2 particles. (The TiB_2 particles appear lighter in color than the aluminum does.) Powder with this morphology should flow well and ensure distribution and wetting of the ceramic within the molten aluminum.

2.2.3 Analysis of Mechanical Alloying Results

For the purpose of optimizing the production of composite powders by mechanical alloying, we adopted from the literature an analytic model describing the kinematics of planetary ball milling. This model helps to identify the process variables that significantly affect the morphology and microstructure of the powders. The following equations are based on the derivations and computations of Burgio et al. (1991), Abdellaoui and Gaffet (1995), and Murty et al. (1995).

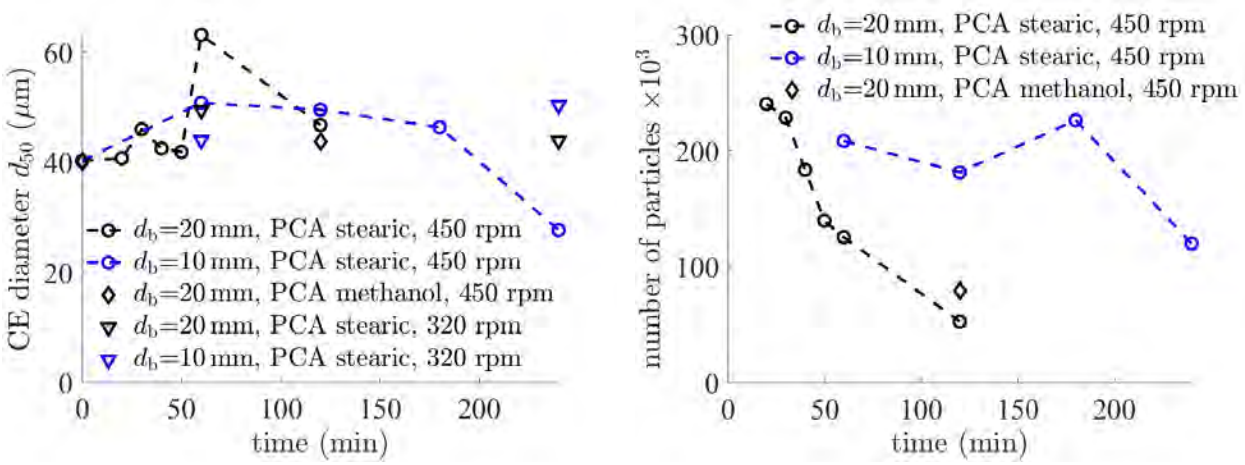

(a) (b)

Figure 8. Effect of ball size, process control agent (PCA), and milling time on morphology of composite particles: (a) Particle diameter; (b) Number of particles per 5 mm^3 sample. (BPR=10)

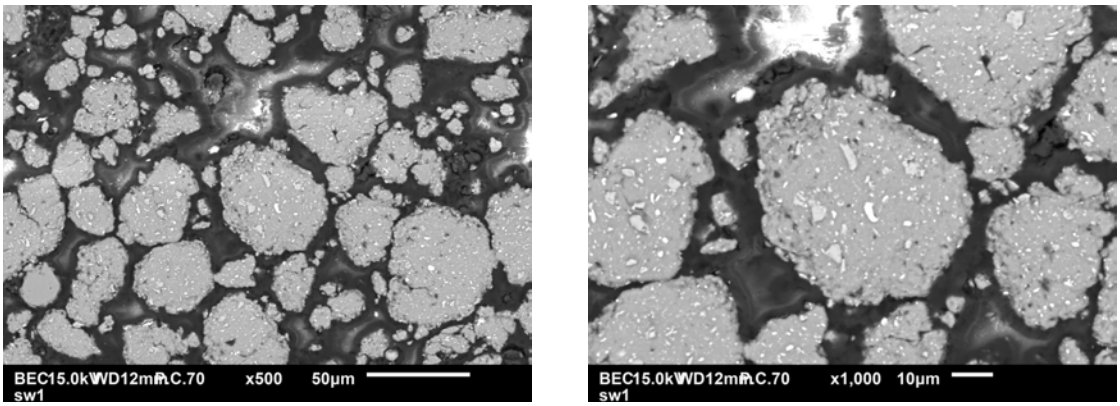

(a) (b)

Figure 9. Sectioned Al-Si10-Mg + 10 wt% TiB_2 particles after 240 min of mechanical alloying: (a) 500× magnification; (b) 1000× magnification. (Mill speed=450 rpm, BPR=10, PCA: stearic acid at 2 wt%.)

The model describes the kinematics of a single ball in a planetary ball mill, with consideration also of the energy dissipated by impacts between balls. For a single ball, the speed at impact with

the wall of the vial is

$$v_{\mathrm{b}} = \sqrt{(r_{\mathrm{d}}\,\omega_{\mathrm{d}})^2 + (r_{\mathrm{v}} - r_{\mathrm{b}})^2\,{\omega_{\mathrm{v}}}^2\left(1 - 2\frac{\omega_{\mathrm{v}}}{\omega_{\mathrm{d}}}\right)}, \tag{1}$$

where r_{b} is the radius of the ball and the other variables are defined in Table 3. The impact energy is then simply

$$E_{\mathrm{b}} = \frac{1}{2} m_{\mathrm{b}}\, v_{\mathrm{b}}^2. \tag{2}$$

The frequency of impacts is approximated as

$$f_{\mathrm{b}} \approx 3.3\,\frac{(\omega_{\mathrm{d}} - \omega_{\mathrm{v}})}{2\,\pi}, \tag{3}$$

based on the time required for the ball to detach from the wall and travel across the vial. From the preceding two equations, the power of a single ball impact, or shock power, is calculated as

$$P_{\mathrm{b}} = f_{\mathrm{b}}\, E_{\mathrm{b}}. \tag{4}$$

Finally, the normalized energy input is calculated by considering the number of balls in the vial, n_{b}, the time of milling, and the mass of the powder:

$$E_{\mathrm{n}} = \frac{P_{\mathrm{b}}\, n_{\mathrm{b}}\, t}{m_{\mathrm{p}}}\,\delta, \tag{5}$$

where δ, the filling parameter, is a number between 0 and 1 that describes the decrease in milling efficiency caused by interaction between the balls. The filling parameter is phenomenologically calculated as

$$\delta = (1 - n_{\delta}^{\epsilon})\,, \tag{6}$$

where n_{δ} approximates the fill ratio of the vial based on the number of balls in the vial and the number of balls that would fill the vial with simple cubic packing, n_{full}:

$$n_{\delta} \equiv \frac{n_{\mathrm{b}}}{n_{\mathrm{full}}}. \tag{7}$$

The parameter ϵ accounts for the fact that the balls do not interfere with each other until they cover about one third of the surface of the vial. For $d_{\mathrm{b}} = 10.3\,\mathrm{mm}$, $\epsilon = 1.497$, and for $d_{\mathrm{b}} = 20.0\,\mathrm{mm}$, $\epsilon = 2.041$.

This model was used to characterize and analyze several of the successful mechanical alloying experiments (Table 4). The results of previous investigators indicate that it is the normalized total energy input, E_{n}, that primarily governs the end product. However, in some cases, it was shown also that this energy must be suppled at a minimum impact energy or shock power. Additional experiments are required in order to draw firm conclusions from our data, but the results indicate that a normalized total energy input of $E_{\mathrm{n}} \geq 43\,\mathrm{W\,h/g}$ is sufficient to form particles with the desired morphology. Furthermore, the results show that impact energy $E_{\mathrm{b}} \geq 0.24\,\mathrm{J}$ and shock power $P_{\mathrm{b}} \geq 18\,\mathrm{W}$ are adequate.

TABLE 4

Mechanical Alloying Process Variables

Mill speed (rpm)	Ball diam., d_b (mm)	Time, t (min)	v_b (m/s)	Impact E, E_b (J/hit)	Shock power, P_b (W)	Normalized E, E_n (W h/g)
450	20.0	240	10.39	1.74	129.23	120.10
450	10.3	240	10.39	0.24	17.65	102.43
320	20.0	240	7.39	0.88	46.47	43.19
320	10.3	240	7.39	0.12	6.35	36.83

2.3 MEASUREMENTS OF POWDER FLOWABILITY

The quality of the powder bed in SLM is determined to a large extent by the properties of the powder itself. (The method of spreading, or recoating, also plays a role.) For a given particle shape, broadening the distribution of particle sizes increases the theoretical packing density, but, even with a distribution of sizes, powder beds with packing densities greater than 0.6 are rarely attained. The property that limits packing density is the ease with which the powder flows, or flowability, when it is spread over the build plane by the recoater blade or roller. Flowability is maximum with monodisperse, spherical particles and decreases with decreasing particle size. As the particle size decreases, the specific surface area of the powder increases, and the magnitude of adhesive and cohesive forces, including van der Waals and electrostatic forces, increases relative to the magnitude of the forces due to gravity, inertia, and contact with the recoater. While increasing the dispersion of the particle size can increase packing density, it also reduces flowability because the area of particle contacts increases and small particles interfere with the rolling of large particles.

The flow characteristics of the as-received metal powders and blended composite powders were characterized by several different measures (Table 5): funnel flow, angle of repose, and Hausner ratio. Funnel flow tests were performed with a Hall funnel and a Carney funnel. Both funnels have a 30° internal cone angle, but the Hall funnel, intended for free flowing powders, has an orifice diameter of 2.5 mm, while the Carney funnel, intended for powders that don't flow freely, has an orifice diameter of 5.0 mm. In these tests, the time for 50 g of powder to flow through the funnel was recorded. In the angle of repose (AOR) test, the powder was poured through the Hall funnel onto a solid brass cylinder with a diameter of 63.5 mm. The angle that the resulting pile made with the horizontal, the angle of repose, is another measure of how the powder flows (with decreasing AOR corresponding to increasing flowabilty). Finally, the Hausner ratio, the powder's ratio of tap density to apparent density, was measured. The apparent density was measured by weighing

25 cm^3 of powder that had been poured into a brass cup using the Hall or Carney funnel. The tap density was characterized by measuring the volume of 50 g of powder that had been mechanically agitated in a graduated cylinder until the sample compacted to a constant volume. Hausner ratios of greater than 1.25 indicate poor flowability.

TABLE 5

Summary of Flow Characteristics of Plain Al-10Si-Mg powder and Blended Composite Powders

Powders Al-Si10-Mg & blends	**Hall flow (s/50 g)**	**Carney flow (s/50 g)**	**Angle of repose (°)**	**Apparent density (g/cm^3)**	**Tapped density (g/cm^3)**	**Hausner ratio**
ECKA Std.	72.8	14.6*	30.1	1.363	1.513	1.11
Valimet Std.	–	–	–	1.335	1.530	1.15
Valimet Coarse	–	10.9	–	1.383	1.527	1.10
LPW Std.	76.3	15.7	31.7	1.300	1.481	1.14
LPW Coarse	57.6	10.8	31.1	1.341	1.502	1.12
Valimet Std. + Starck-F-10%	–	–	–	1.172	1.501	1.28
LPW Std. + US Nano-10%	–	–	–	1.211	1.587	1.31
LPW Std. + Starck-F-10%*	–	–	–	1.141	1.454	1.27
LPW Coarse + US Nano-10%*	–	–	–	1.301	1.520	1.17

Admittedly, none of the tests described in the previous paragraph can precisely predict how a powder will flow in an actual SLM machine because they do not characterize the powder under the conditions of shear flow that the recoater imposes. However, the results of these tests do serve as valuable indicators of the flow characteristics during recoating.

The low density of aluminum notoriously causes poor flow with particles of diameter less than about 100 μm, and our powders obeyed this trend (Table 5). The plain aluminum powders of

standard size all exhibited acceptable Hausner ratios (< 1.25), but the Hall flow was either very slow or nonexistent. In fact, the standard Valimet powder, the very same powder presently used by Group 72 in the MIT LL production machine, did not flow through either the Hall funnel or the Carney funnel. Of the standard powders, the ECKA powder exhibited the best flow characteristics by all three measures, which we attribute to its particles being larger than those of the Valimet powder and more spherical than the LPW particles. As we expected, the Coarse powders, comprised of larger particles, flowed better than the Standard powders did, but the even the Valimet Coarse would not flow through the Hall funnel. For future development of composite powders, the LPW Standard powder was selected because it flows reasonably well and is readily available in the U.S.

The blending of the aluminum powders with the comparatively fine ceramic powders at 10 wt% caused flowability to decrease substantially (Table 5). None of the blends would flow through either funnel, and only the LPW Coarse Al-Si10-Mg blended with U.S. Nano TiB_2 displayed a Hausner ratio less than 1.25. We attribute the poor flow characteristics to the blends' bimodal distribution of particle size: the small ceramic particles occupy the spaces between the aluminum powders, increasing rolling resistance and jamming the flow.

The most relevant measures of flowability take place in an actual SLM machine or an experimment that simulates powder recoating. Despite differences in measured flow properties, all the plain aluminum powders could be spread by the recoater of the SLM testbed in sufficiently thin and uniform layers. On the other hand, the recoater could not spread any of the blended powders. (The SLM testbed is described in Section 4.1.)

For rapid, direct evaluation of powder recoating characteristics, a simple manual test was devised. Thin plates of forged Al-12Si were milled flat and bead blasted with a 50 μm bead size to promote adhesion of powder to the plate. Next, two sections of tape, each about 75 μm thick, were applied to either side of the plate to serve as shims. We then placed small samples of powder at one end of the plate and attempted, by hand, to rake the powder over the plate with a beveled steel blade designed for SLM recoating. The blade successfully spread all the plain aluminum powders (Figure 10), but could not spread any of the blended powders in the thin, uniform layers that would maximize melt pool stability.

By qualitative measures, the composite powders fabricated by mechanical alloying appear to flow much better than the blended powders do. They readily roll down the wall of their container at angles for which the blended powders would remain firmly adhered to the wall. The improvement in flowability is caused primarily by the migration of the ceramic particles to the interior of the aluminum particles, which eliminates the blend's initial bimodal distribution of particle sizes. While powders produced by mechanical alloying are not as spherical as gas atomized powders, they typically have very narrow size distributions, which also favors flow. We are presently tuning the alloying parameters and upscaling the process so that samples can be fabricated for flowability and laser consolidation experiments.

Figure 10. 75 μm layer of plain Al-Si-10Mg powder manually spread on Al-12Si substrate with a beveled steel blade.

This page intentionally left blank.

3. MATHEMATICAL MODELING OF LASER CONSOLIDATION

Laser consolidation by SLM is exceptionally complex because it involves multiple types of physics and numerous process variables. The physics inlude phase changes, mass transfer, and several modes of heat transfer (Figure 11a). The process variables include both laser parameters (beam diameter, velocity, and hatch pattern) and powder bed parameters (layer thickness, packing density, absorptivity, conductivity, and initial temperature), as illustrated in Figure 11b.

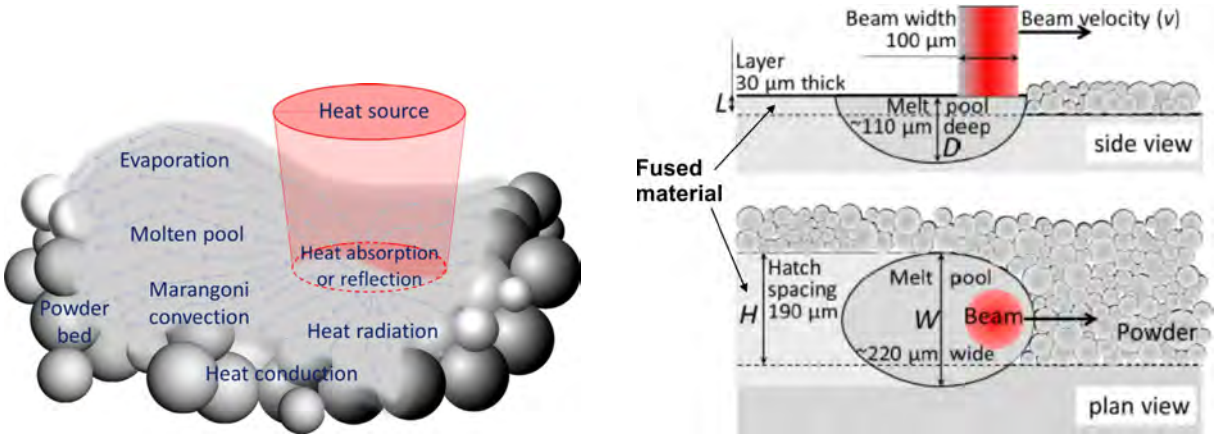

(a) (b)

Figure 11. Schematics of laser heating and melt pool formation during SLM: (a) Multiple types of heat transfer occur simultaneously; (b) SLM process parameters include beam size, beam velocity, powder layer thickness, and hatch spacing.

Because of the complexity of the SLM process, scaling relations, analytic models, and numerical models of the laser heating process have been developed for the purpose of planning experiments, interpreting experimental results, and optimizing process parameters. Specifically, the goal is to relate the machine and powder bed parameters to the melt pool characteristics and thermal history. By controlling melt pool temperature and aspect ratio, we can prevent defects due to lack of fusion (energy too low), keyholing, evaporation of alloying elements (energy too high), and melt pool balling (scan velocity too high). In addition, predictions of melt pool dimensions can be used to determine hatch spacing and powder layer thickness for new materials or new process parameters. At the level of microstructure, local thermal gradients, solidification velocities, and cooling rates can be manipulated to engineer grain type, size, composition, and orientation. (For example, equiaxed, fine grained microstructures can enhance fatigue strength, promote even distribution of reinforcement particles, and prevent hot tearing during solidification.) Finally, residual stresses

that cause defects, warping, and poor part performance can be reduced by designing scan strategies that produce uniform heating and cooling.

Modeling can also predict how the ceramic content of the powder will change the melt pool characteristics. The effect of powder bed properties such as packing density, absorptivity, and effective thermal conductivity can be simulated as a function of ceramic content, facilitating navigation of the numerous trade-offs associated with SLM of multimaterial, multiphase powder beds. For example, on the one hand, the high absorptivity of the ceramic phase should reduce the laser power required (aluminum has very low absorptivity). But, on the other hand, an increase in melt pool temperature may be necessary to counteract the increase in viscosity caused by the ceramic particles, which can impede the wetting of the previously consolidated layer by the melt pool.

3.1 GOVERNING EQUATIONS

The laser beam, with radius r, moves at constant velocity v in the x-direction as it scans over the surface of the powder bed, which lies in the $(x,\, y)$ plane. It is represented by a Gaussian intensity distribution in the $(x,\, y)$ plane,

$$I(x, y, t) = \frac{A \cdot P}{\sigma\, \pi\, r^2} \exp\left(-\frac{(x - v\, t)^2 + y^2}{\sigma\, r^2} \right) \equiv I_0 \exp\left(-\frac{(x - v\, t)^2 + y^2}{\sigma\, r^2} \right), \tag{8}$$

where P is the power of the laser beam at the surface of the powder bed, A is the absorptivity of the powder, I_0 is the peak intensity of the beam, and σ describes the shape of the intensity distribution. Assuming that the heat transfer is dominated by thermal conduction, the heat diffusion equation can be written as

$$\rho\, c_p \frac{\mathrm{d}T}{\mathrm{d}t} - \mathrm{Div}\,(k\, \mathrm{Grad}\, T) = I\,(x,\, y)\, \delta\,(z)\,, \tag{9}$$

where $\rho = \rho(T)$ is the apparent mass density, $c_\mathrm{p} = c_\mathrm{p}(T)$ is the specific heat capacity, $k = k(T)$ is the thermal conductivity, and $\delta\,(z)$ is a delta function at the surface of the powder bed.

3.2 ANALYTIC MODELING

We model the powder bed as semi-infinite and approximate the material properties to be independent of temperature. At steady state, the heat equation can be solved for $t = 0$, when the laser beam is at $x = 0$, by superimposing the Gaussian intensity distributions that occurred at earlier times $t' = 0 \to -\infty$ when the beam was located at coordinates $(x',\, y')$. The solution is found by by a standard Green's function method and then integrated analytically over x' and y'. The solution takes the form of an amplitude term that does not vary with position multiplied by a dimensionless shape function:

$$T\,(x,\, y,\, z) - T_0\,(x,\, y,\, z) = \underbrace{\frac{A \cdot P}{k\, r}}_{\text{dimension } T} \times \underbrace{f\left(\frac{x}{r},\, \frac{y}{r},\, \frac{z}{r},\, \frac{v\, r}{\alpha},\, \sigma \right)}_{\text{dimensionless shape function}}. \tag{10}$$

The amplitude term increases with increasing absorbed power and decreases with increasing thermal conductivity and beam size. The shape function, f, depends only on the shape of the beam's intensity profile and the dimensionless velocity, $\overline{v} \equiv v\,r/\alpha$, where $\alpha = k/\rho c_\mathrm{p}$ is the thermal diffusivity. The dimensionless velocity, also known as the Péclet number, characterizes the ratio of heat flow by transport to heat flow by diffusion. For a given thermal conductivity and beam intensity, f completely determines the distribution of temperature in the material. Similarly, a dimensionless group describing the power that is required for the laser melting of metals can be defined by dividing the amplitude term by the temperature rise: $\overline{P} \equiv \dfrac{A \cdot P}{k\,r} \dfrac{1}{(T_\mathrm{m} - T_0)}$.

We numerically integrate and evaluate the shape function along each of the coordinate axes to determine the maximum temperature in the material and explore the shape of the temperature distribution as a function of the dimensionless velocity. As expected, in the y and z directions, the temperature is a maximum at the center of the beam and at the surface of the material ($y = 0$, $z = 0$). However, in the x-direction, the maximum temperature shifts further behind the center of the beam as $\overline{v}$ increases (Figure 12). As the beam velocity increases, the time for heat flow by conduction decreases, and the effect of heat input at prior times and locations begins to dominate over the effect of thermal conduction.

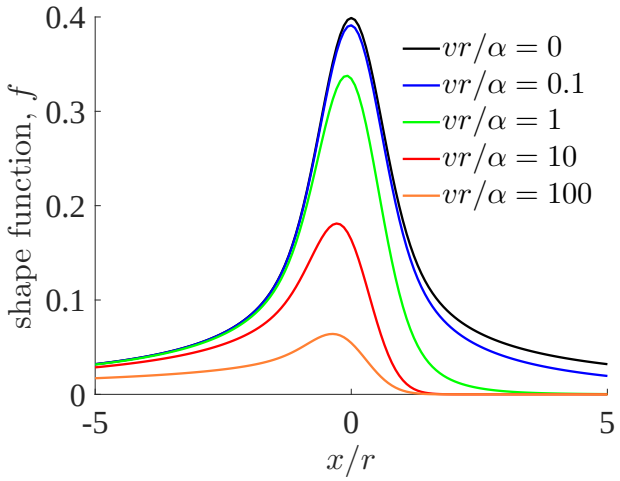

Figure 12. Plot of the shape function f that predicts the distribution of temperature in the powder bed as a function of dimensionless velocity, $\overline{v} = v\,r/\alpha$. Along the x-axis, the direction of laser travel, the peak temperature lags behind the location of the beam ($x = 0$). As $\overline{v}$ decreases, f and thus the temperature do not increase monotonically but approach a constant distribution.

Considering a powder bed composed of plain Al-Si10-Mg, we now integrate over the surface of the powder bed to solve for $T(x, y, z = 0)$ as a function of laser power and scan velocity. Maintaining a constant areal energy density, $E_\mathrm{A} \equiv P/(v \cdot 2r)$, we plot the predicted temperature distribution at three different powers and velocities (Figure 13). Here, although the energy density is the same in each case, the melt pool dimensions, aspect ratio, and peak temperature increase with increasing scan velocity. Referring to the temperature solution (Equation 10), we note that the amplitude term increases linearly with increasing laser power, but the effect of increasing the scan velocity is hidden within the shape function (which includes an exponential term). Because Al-Si10-Mg has a high thermal diffusivity, $\alpha = 6.2 \times 10^{-5}\,\mathrm{m}^2/\mathrm{s}$, $\overline{v}$ is small at these scan velocities, ranging from $v\,r/\alpha = 0.32$ to $v\,r/\alpha = 1.28$. Therefore, as shown in Figure 13, the shape function hardly changes as the scan velocity increases in this range. With the amplitude term increasing linearly and the shape function remaining approximately constant, the temperature and thus the melt pool dimensions must increase as the laser power is increased at constant energy density.

The key result of this analysis is the nonlinear relationship between $\overline{v}$ and the distribution of temperature in the material. At constant laser intensity, when $\overline{v}$ decreases in the range of $\overline{v} = 1{-}100$, the maximum temperature in the material increases logarithmically, but thereafter there is little benefit in increasing $\overline{v}$. Similarly, the size of the melt pool, indicated by the width of the temperature distributions at a given value of f, does not increase significantly for $\overline{v} \lesssim 1$. This result explains the limitations in laser consolidation of increasing energy density by decreasing laser scan velocity. Rather, it is preferable to increase laser power, particularly for materials with high thermal diffusivity, such as the aluminum matrix composites being developed here.

3.3 NUMERICAL MODELING

Analytic models and scaling relations can uncover the fundamental relationships between process parameters, microstructure, and properties, but it is very difficult to derive analytic solutions for cases with finite geometry or modes of heat transfer in addition to pure conduction. Therefore, we are presently developing numerical models of laser consolidation that can predict melt pool characteristics and thermal history under conditions more complex than the idealized case of Section 3.2. Some of the effects that can readily be incorporated into numerical models are convective heat transfer, thermal radiation, phase changes, temperature dependence of material properties, and multiple scan tracks.

We have built the numerical models at the continuum level, where computational cost is reasonable, using the finite element method to solve the heat equation (Equation 9). The intensity of the laser beam is described by the same Gaussian form previously given by Equation 8. A critical initial step in developing a numerical model is to determine a domain size and level of discretization that provides an appropriate balance between accuracy and computation time. Based on the analytic predictions of the size of the heat-affected zone, a domain size of $L_x = 1.52\,\mathrm{mm}$, $L_y = 0.8\,\mathrm{mm}$, and $L_z = 0.4\,\mathrm{mm}$ was chosen for the simulation of single scan tracks (Figure 14).

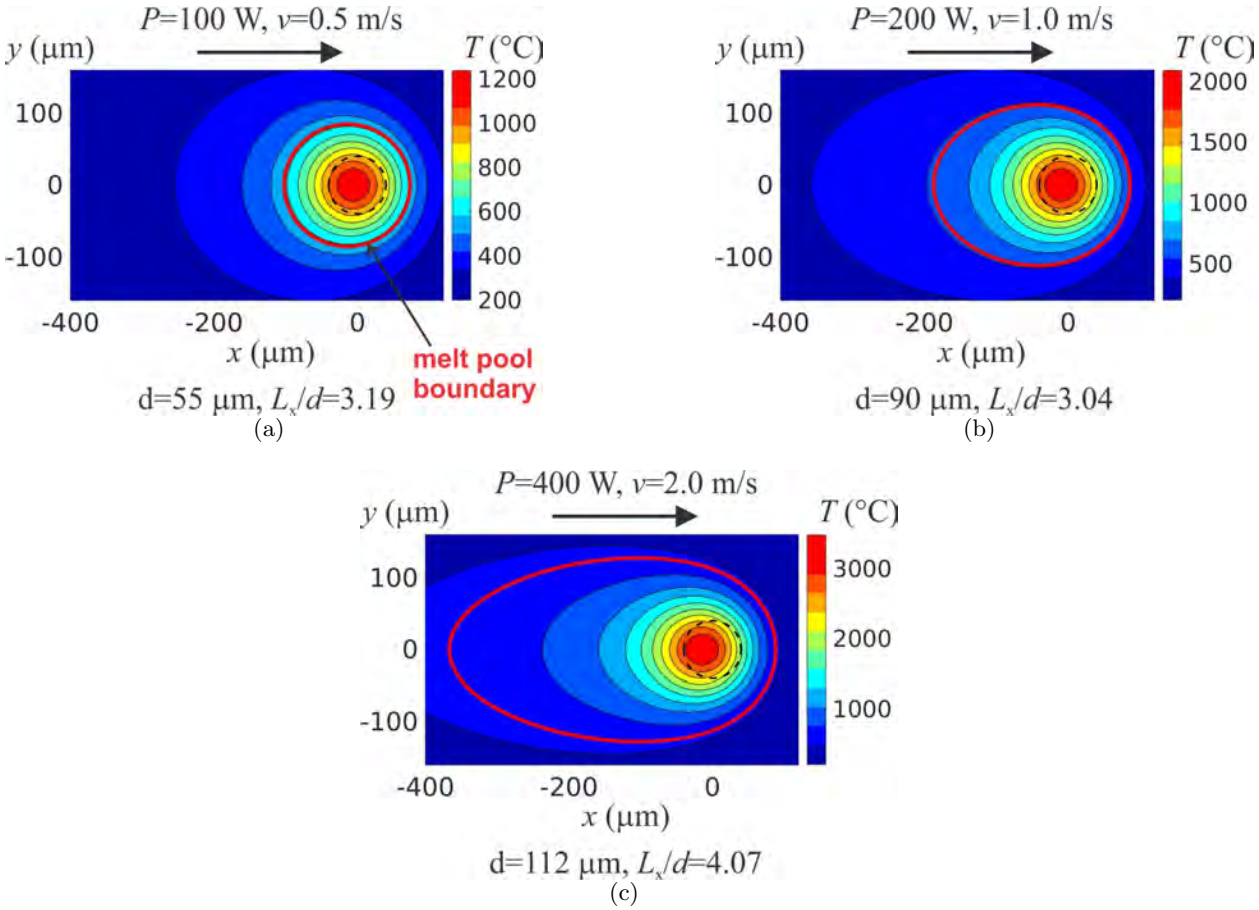

Figure 13. Analytic model predictions of melt pool size and temperatures $T(x, y, 0)$ for plain Al-Si10-Mg: Melt pool dimensions, aspect ratio, and maximum temperature increase with increasing laser scan velocity at constant areal energy density, E_A (for $d_{beam} = 80\ \mu m$ and $A = 0.35$): (a) $v\,r/\alpha = 0.32$; (b) $v\,r/\alpha = 0.64$; (c) $v\,r/\alpha = 1.28$. (Dashed circle indicates position of laser beam spot.)

Discretizing this domain with linear heat transfer elements (Abaqus DC3D8), we found that the analytic solution for the steady state temperature distribution could be matched with an element size $h = 1/5 \times d_{beam}$ (20 μm, in this case) and a scan length $L_{scan} = 0.60$ mm (Figure 15). Additional simulations showed that the time increment should be limited so that the maximum change in temperature during an increment does not exceed 25 °C.

The preprocessing and postprocessing of these numerical simulations were all scripted in Python so that further parametric studies can be readily carried out. With the numerical meth-

ods validated, we will next add the capabilities to simulate surface heat losses, phase changes, temperature dependent material properties, and thermal cycling caused by adjacent scan tracks.

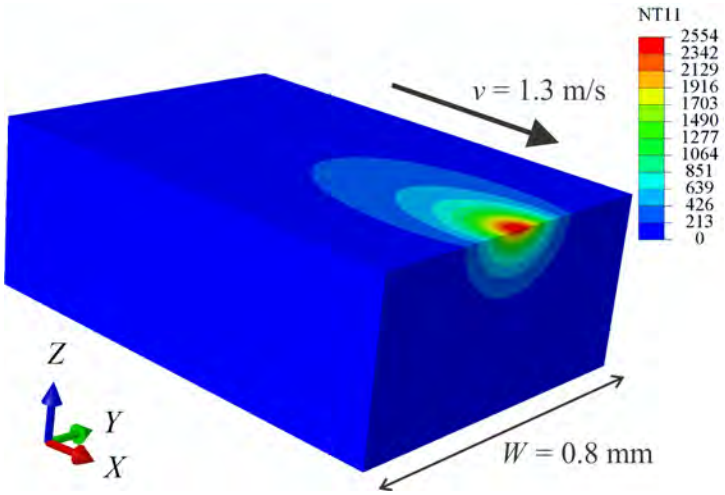

Figure 14. Numerical simulation of single track melting of plain Al-Si10-Mg ($P = 370\,\mathrm{W}$, $v = 1.3\,\mathrm{m/s}$, $d_{\mathrm{beam}} = 100\,\mu m$, $A = 0.35$, and element size $h = 10\,\mu m$).

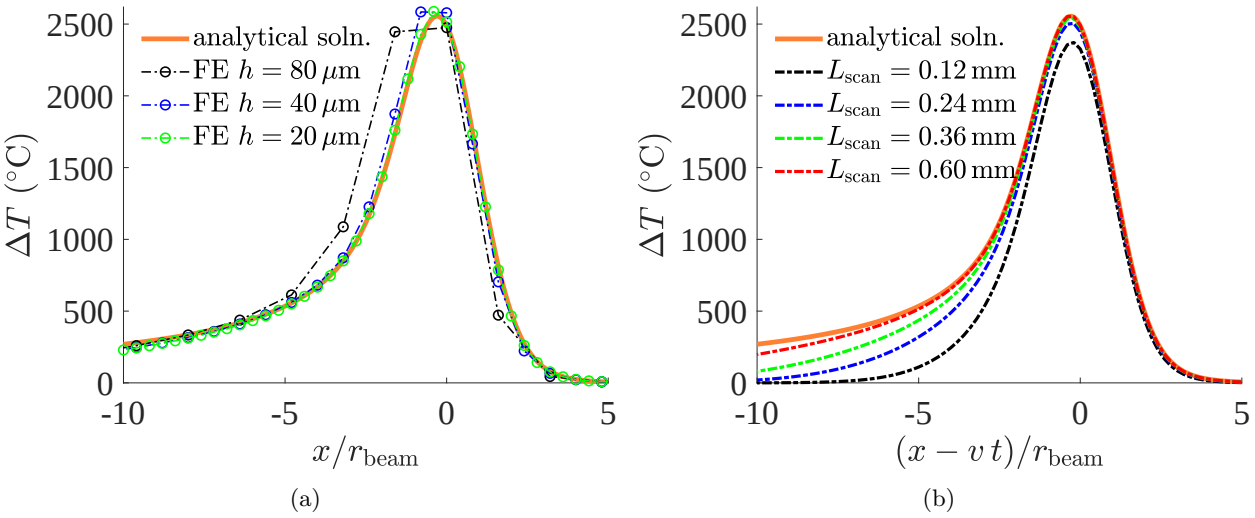

Figure 15. Comparison of the melt pool temperatures predicted by analytic and numerical models as a function of element size (a) and laser scan length (b). Steady state analytic solution is approached at $h = 20\,\mu m$ *and* $L_{\text{scan}} = 0.60\,mm$.

This page intentionally left blank.

4. LASER CONSOLIDATION

Laser consolidation is being performed with a custom built SLM testbed from Aconity3D in Germany (Figure 16). Unlike commercial machines, the SLM testbed allows selection of process parameters over a wide range of laser parameters, scan strategies, powder bed temperatures, and recoating parameters. The selection of these parameters is being guided by the models of Section 3 that predict melt pool characteristics and thermal history as a function of process parameters and powder composition.

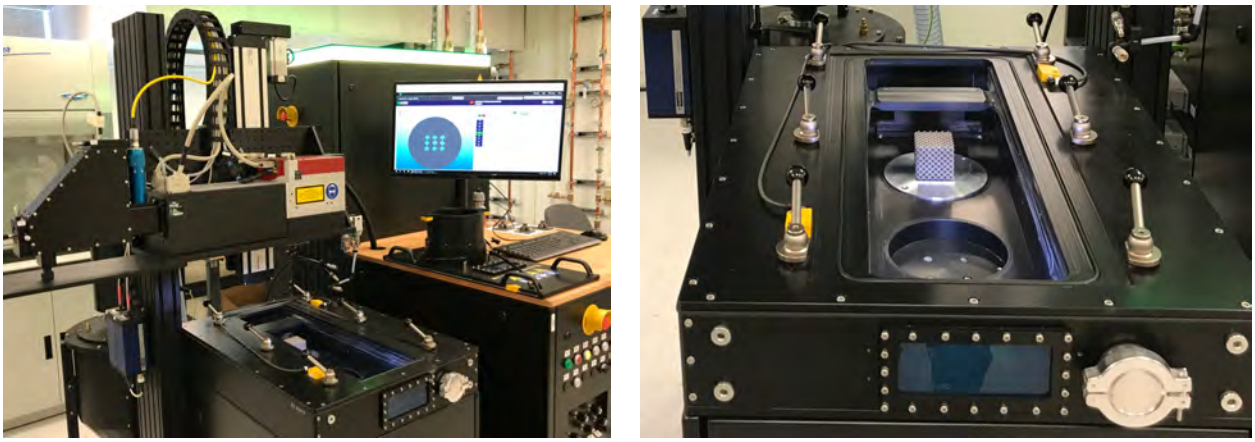

(a) (b)

Figure 16. Aconity SLM research system: (a) Build chamber, CW fiber laser, scan head, and control cabinet; (b) Close-up of build chamber, showing powder supply cylinder, build platform, and powder recoater (front to back).

4.1 DESCRIPTION OF SLM TESTBED

The SLM testbed was installed at MIT LL in May of 2018. It is an open access system designed to our specifications for the development of new materials for SLM. Process conditions can be broadly tuned to prevent the occurrence of defects and produce desirable microstructures. The testbed's key features include:

- Inert build chamber with recirculation and filtering that enable the processing of highly reactive materials such as aluminum alloys. (Flow rate of inert gas across the build plate is controlled to remove weld fumes and splatter.)

- Continuous wave fiber laser with maximum power of 420 W
- On-the-fly adjustment of laser beam power and diameter (d_{beam}=80–500 μm)
- Full control of the laser scan path
- Powder bed preheating up to 500 °C
- Size reduction kits for the build platform and supply platform (d=55 mm) that enable the processing of small quantities of powder (< 100 g of powder for 1 cm build height)
- Interchangeable recoater blade (steel, rubber, or carbon fiber brush) and full control of powder layer thickness, blade height, and blade velocity
- Melt pool temperature sensing with two pyrometers
- Support for additional sensors for process monitoring and addition of feedback control

4.2 LASER CONSOLIDATION OF SINGLE TRACKS OF POWDER

In the first set of experiments, single lines of the matrix Al-Si10-Mg powder (LPW Standard) were consolidated with the SLM testbed at various laser powers and scan velocities (Figure 17). For a given material, this type of experiment is a highly efficient way to estimate the range of process parameters that can be used to fabricate bulk samples with minimal defects. Within this process window, the single lines, or tracks (similar to laser weld beads), exhibit the following characteristics:

- Smooth, uninterrupted profiles when viewed from above
- Sufficient penetration into the substrate to ensure a strong connection
- Sufficient height above the substrate to build in the vertical direction
- An angle of connection with the substrate of close to 90°

In addition to the determination of laser power and scan velocity, single track experiments can also provide estimates of the optimal hatch spacing and powder layer thickness, based on the dimensions of the weld bead's profile.

Following the procedure described in Section 2.3, we prepared single layer samples by manually raking 75 μm layers of Al-Si10-Mg powder over an Al-12Si substrate. Single lines of powder were then consolidated at powers of 95–380 W and scan velocities of 50–2000 mm/s. The scan lines were all 7.5 mm long and were spaced at 1.5 mm intervals. The results of these experiments show that the process window for plain Al-Si10-Mg comprises laser powers of about 200–400 W at velocities that increase with increasing laser power (Figure 17). Outside this window, at high powers and

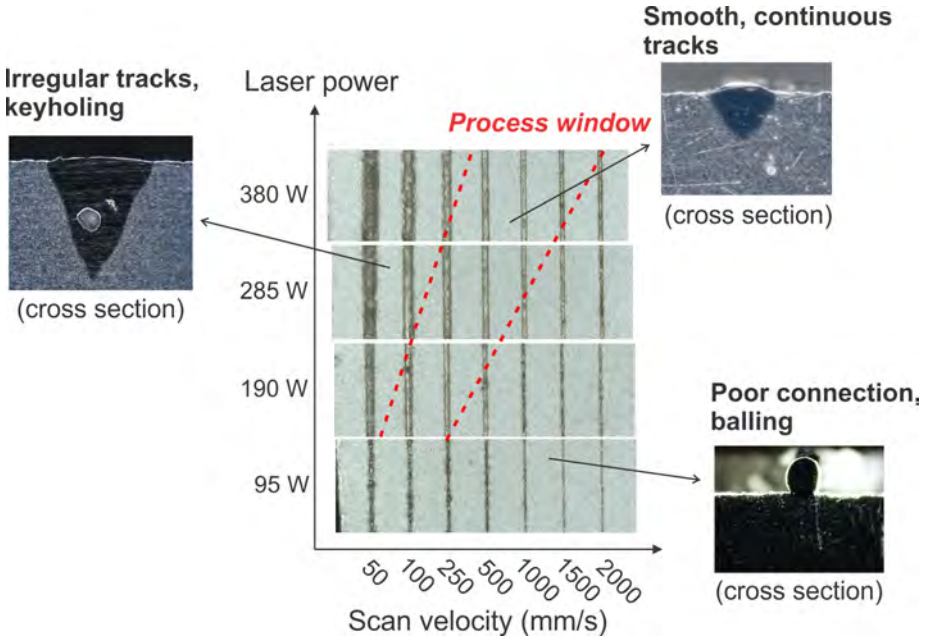

Figure 17. Process window for plain Al-Si10-Mg powder determined from single track melting experiments (75 μm powder layer spread on Al-12Si substrate).

low velocities, the melt pool transitioned from conduction mode to keyhole mode. In keyhole mode, the melt pool temperature exceeds the alloy's boiling point, and evaporation of the liquid metal and high vapor pressures cause a deep channel to form within the melt pool. After the laser passes, the molten metal fills in the channel, leaving behind a flat weld bead and often pores where the channel did not fully close ("keyhole pores," as shown in Figure 17, left). On the other hand, outside the window at low powers and high velocities, the weld bead exhibits irregularities and poor connection to the substrate (Figure 17, right). Here, the melt pool failed to wet the substrate completely because surface tension spheroidized the liquid and the substrate did not melt sufficiently.

With the process window for plain Al-Si10-Mg identified, we are now ready to characterize similarly the composite powders fabricated by mechanical alloying. We expect that the presence of the ceramic phase will alter a number of the process variables, including powder bed packing density, laser absorptivity, and melt pool viscosity. Changes in the process window correlated with changes in the ceramic content of the powder bed will be strong indicators of the nature of the physics underlying the microstructure and properties of the consolidated composite materials.

4.3 LASER CONSOLIDATION OF BULK SAMPLES (DENSITY CUBES)

Next, we fabricated bulk samples to characterize quantitatively the level of defects in the consolidated matrix alloy. In small samples, defects can be caused by keyhole melting, balling of the melt pool, and insufficient remelting of previously consolidated layers. (In larger samples or parts, defects can also be caused by residual stresses.) No matter their cause, however, defects of this type are manifested as porosity in the solid material, which can be measured accurately by the Archimedes method (using samples called "density cubes" because mass density is actually measured). We therefore fabricated $1\,\mathrm{cm}^3$ cubes using various laser powers and scan velocities (Figure 18a).

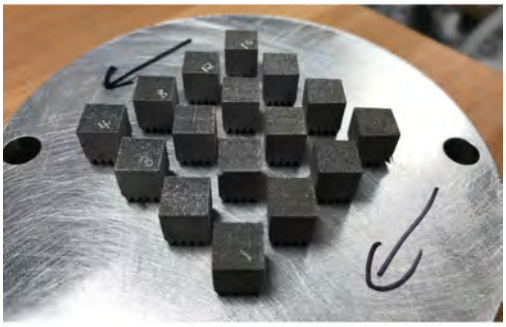

(a)

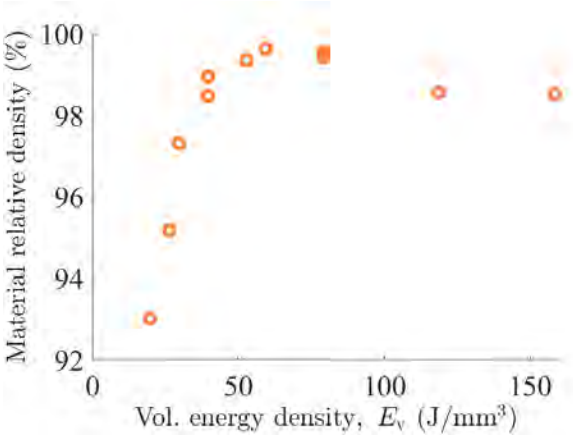

(b)

Figure 18. Laser consolidation of bulk samples of Al-Si10-Mg: (a) 1 cm³ density cubes built with P=190–380 W and v=500–2000 mm/s; (b) The relative density of the samples peaks at volumetric energy densities in the range E_V=52.8–79.2 J/mm³.

The process parameters used for the density cubes were selected based on the predicted melt pool dimensions, as well as the results of the single track consolidation experiments: $P = 190{-}380\,\mathrm{W}$, and $v = 500{-}2000\,\mathrm{mm/s}$. The powder layer thickness was $t_{\mathrm{powder}} = 30\mu\mathrm{m}$, and the hatch spacing was $h_{\mathrm{beam}} = 160\,\mu\mathrm{m}$. The laser scan direction was rotated $\pm 90°$ after each layer, and a 5 mm island scan strategy was used, meaning that consolidation occurred by 5 mm squares in a checkerboard fashion. After consolidation, the samples were cut off the build plate, and the support structures were removed by milling. The density of each sample was then measured by the Archimedes method (OHAUS Explorer EX), permitting the calculation of the relative density, $\rho_{\mathrm{rel}} \equiv \rho/\rho_{solid} \times 100$. The results show that relative densities in excess of 99% were achieved with the

matrix alloy (Figure 18b). Although energy density is an imperfect measure (as we demonstrated in Section 3.3), it is convenient and common to plot the relative density as a function of the volumetric energy density,

$$E_{\mathrm{V}} = \frac{P}{v\, h_{\mathrm{beam}}\, t_{\mathrm{powder}}}. \tag{11}$$

For $\rho_{\mathrm{rel}} > 99\%$, the volumetric energy density is in the range of 52.8–79.2 J/mm^3, corresponding to combinations of laser power and scan velocity of ($P = 190\,\mathrm{W}$, $v = 500\,\mathrm{mm/s}$), ($P = 285\,\mathrm{W}$, $v = 1000\,\mathrm{mm/s}$), and ($P = 380\,\mathrm{W}$, $v = 1000{-}1500\,\mathrm{m/s}$). Compared with the results of the single track consolidation experiments in Figure 17, these combinations of power and velocity are all within the determined process window, validating the predictions of the single track experiments.

Moreover, the robust, nearly defect-free microstructure of the samples was confirmed by optical microscopy. Bulk samples were sectioned both horizontally and vertically with a diamond saw and then mounted, ground, polished, and etched with Keller's reagent. The micrographs reveal individual melt pools (Figure 19a) and consolidated layers (Figure 19b), with the small amount of porosity appearing as dark spots.

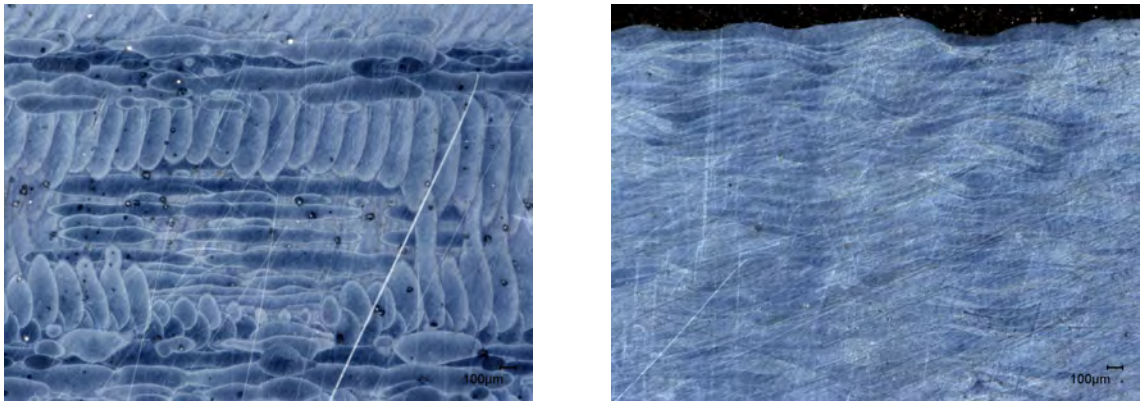

(a) (b)

Figure 19. Optical microscopy of bulk samples of Al-Si10-Mg (etched with Keller's reagent): (a) Sectioned horizontally (parallel to the build plane), revealing individual melt tracks at ±90°; (b) Sectioned vertically (normal to the build plane), revealing the layers of consolidated powder.

This page intentionally left blank.

5. CONCLUSION

During FY 2018, remarkable progress was made toward the goal of inventing high performance structural materials for additive manufacturing. In the process, tremendous leave-behind capability was also developed that will spur additional research at MIT LL in the areas of new materials and processes for additive manufacturing.

FY 2018 saw completion of the Metals AM Research Lab (D-319). With substantial funding from this project, we purchased and installed all the major equipment required for powder fabrication, consolidation by SLM, sample preparation, characterization of powders, and metallography of consolidated materials. Along the way, countless infrastructure and engineering hurdles were overcome, and many procedures were set in place to mitigate the hazards associated with handling fine, explosive powders and working with a high power laser.

The research this past year progressed on all three fronts: development of feedstock powder, SLM process modeling, and laser consolidation. We demonstrated the production of composite powders optimized for spreading and consolidation by an SLM machine. Analytic and numerical models of laser consolidation were constructed to predict process parameters and to improve our understanding of the effects of the various process variables on the consolidated material's microstructure and properties. With the freshly completed SLM testbed, we identified the process window for consolidation of the matrix alloy and demonstrated 99.6% dense consolidation within this process window (much higher than the relative density of most metals manufactured by the traditional method of casting).

The focus in FY 2019 will shift to production of larger samples of powder and consolidation of bulk MMC samples. Using this year's results and kinematic models of ball milling, the production of ceramic-reinforced powders will be upscaled, and the flow and packing properties of the powder will be optimized. Bulk samples will then be consolidated from these composite powders. The microstructure and properties of the bulk MMCs will be characterized by microscopy, density measurement, and indentation testing. In parallel, the numerical modeling of laser consolidation will be extended to simulate multiple scan tracks and layers of powder so that the effects of track overlap and thermal cycling can be predicted.

The development of printable metal matrix composites will greatly enhance the performance of a wide variety of airborne sensor and communication systems. Structural components fabricated from MMCs will be stiffer and more stable than those fabricated from unreinforced metals, and reductions in structural weight will enable increases in payload capacity. In addition, reducing weight will alleviate the need for complex vibration isolation systems, decreasing system weight further and significantly reducing cost. The ability to tune material properties by varying ceramic content will increase design freedom by enabling thermal expansion matching of components and selection of the optimum balance of stiffness and toughness. At the conclusion of the program, we envision transferring the materials and processes to production SLM machines at MIT LL and

other organizations, thereby opening up many new applications for these impressive, yet currently vastly underused, materials.

A RELATED PUBLICATIONS

E. M. Parsons,"Lightweight cellular metal composites with zero and tunable thermal expansion enabled by additive manufacturing: Modeling, manufacturing, and testing," Composite Structures, 2018, *under review.*

This page intentionally left blank.